Dissociative ionization of H_2 in an attosecond pulse train and delayed laser pulse

Feng He and Uwe Thumm
James R. Macdonald Laboratory, Kansas State University, Manhattan, Kansas 66506-2604, USA
(Received 22 January 2010; published 17 May 2010)

The ionization of H_2 in a single attosecond extreme ultraviolet (XUV) pulse generates a nuclear wave packet in H_2^+, which is entangled with the emitted photoelectron wave packet. The nuclear wave-packet dynamics can be observed by dissociating H_2^+ in a delayed IR laser pulse. If H_2 is ionized by a sequence of XUV pulses of an attosecond pulse train, whether or not the corresponding sequence of nuclear wave packets in H_2^+ is detected as a coherent or incoherent superposition depends on whether and how the photoelectrons are observed. We simulate the nuclear dynamics in this XUV-pump–IR-probe scenario and analyze our numerical results for both single attosecond pump pulses and pump-pulse trains of different lengths and temporal spacings between individual XUV pulses. By superimposing nuclear wave packets in H_2^+ generated by individual pulses in the pump-pulse train incoherently, we calculate proton kinetic energy release spectra that are in good qualitative agreement with the recent experiment of Kelkensberg *et al.* [Phys. Rev. Lett. **103**, 123005 (2009)].

DOI: 10.1103/PhysRevA.81.053413 PACS number(s): 32.80.Rm, 33.80.Rv, 42.50.Hz

I. INTRODUCTION

Recent advances in laser technology have begun to allow the observation in real time of the motion of electrons in atoms, molecules, and solids [1–3]. Although electrons in light atoms and molecules move at a time scale of hundreds of attoseconds (1 as $= 10^{-18}$ s), more than one order of magnitude faster than the carrier period of typical 800-nm IR laser light (2.7 fs), intense short IR laser pulses constitute the enabling tool for experiments with sub-fs time resolution. For example, by irradiating a (usually gaseous atomic) target with intense multicycle carrier-envelope-phase (CEP) stabilized IR pulses, the IR electric field can move target electrons along "rescattering" trajectories, leading to the generation of higher harmonics (HHs) at odd multiples of the IR frequency ω_{IR} [4–7]. By appropriate spectral filtering, HHs can be coherently superimposed over a sufficiently wide spectral range to form coherent optical wave packets, with pulse widths in the 100-as range [8–10]. These attosecond pulses are phase locked to the primary IR pulse. Typically, a single attosecond pulse (SAP) is generated during every half cycle of the driving IR pulse, leading to an attosecond pulse train (APT) whose SAP intensities follow the shape of the IR pulse.

The combination of a SAP or APT with a time-delayed CEP-stabilized IR pulse in pump-probe experiments is capable of tracing electron dynamics in excited atoms and molecules. In such experiments, each SAP generates a coherent superposition of excited atomic or molecular states, that is, a moving quantum mechanical wave packet, whose evolution is monitored by the delayed IR probe pulse. For atomic targets, sub-fs-pump–IR-probe experiments can resolve in time the decay of inner-shell vacancies (providing an alternative, real-time measurement of autoionization linewidths) [11] and laser-induced tunneling ionization [12]. Such experiments can also measure with suboptical-cycle resolution the carrier-electric field of an IR pulse (by IR-streaked XUV photoemission spectroscopy) [13], and analyze the phase variation in interfering photoelectron wave packets that are emitted by subsequent XUV pulses of an APT [14].

For molecular targets, the situation is more complex than for atoms due to the added nuclear degrees of freedom. Each SAP in the APT not only emits a photoelectron wave packet, but also generates a ro-vibrational nuclear wave packet in the molecular ion [15]. Since the electronic and nuclear motion in the neutral target molecule are correlated (entangled), the nuclear and photoelectron wave packets are likewise entangled [16]. Applying a time-delayed IR field to dissociate or ionize the molecular ion, the fragment kinetic energy release (KER) can be measured as a function of the delay Δt and images the evolution of the nuclear motion in the molecular ion. Since subsequent SAPs in the APT are phase coherent, nuclear and electronic wave packets emitted by different SAPs interfere. One may thus expect that KERs measured in experiments with SAPs and APTs are qualitatively different, their difference being related to the degree of coherence between successively launched nuclear wave packets in the molecular ion and the different spectral profiles of SAPs and APTs [17]. Since photoelectrons carry phase information, the degree of coherence in the observed KER in an APT-delayed–IR-pulse experiment will depend on whether and how photoelectrons are detected in coincidence with molecular fragments. Without the observation of coincident photoelectrons, we anticipate the KER to be devoid of coherence effects between subsequently launched nuclear wave packets, whereas coherence effects are expected to be most prominent if photoelectrons are detected in extremely narrow momentum bins and coincident with molecular fragments.

In this article, we simulate fragment energy spectra for different XUV-pump–IR-probe scenarios, considering either SAPs or APTs in the pump step, and discuss our results for the limiting cases where coincident photoelectrons are detected with perfect momentum resolution or not detected at all. We will discuss interference effects in the coherent superposition of nuclear wave packets produced by successive SAPs in an APT, characterize dissociating nuclear wave packets with regard to their temporal evolution and stationary-vibrational state distribution, and compare our numerical findings with a recent experiment [18]. The H_2 molecule will serve as prototypical system in all numerical simulations. After single ionization of the neutral molecule out of its electronic and vibrational ground state by a SAP or APT, we examine the

nuclear motion in H_2^+ by dissociation of the molecular ion in a time-delayed IR laser field and analyze the fragment energy spectrum both in the time domain [19,20] and with regard to its (quantum-beat) frequency spectrum [21–23]. In particular, we examine proton energy spectra in view of the manifestation of interference of H_2^+ nuclear wave packets that are formed by different attosecond pulses in the APT.

Following this introduction, we review our theoretical model in Sec. II. We discuss our numerical results in Sec. III and present a summary and outlook in Sec. IV. Unless stated otherwise, we use atomic units throughout this work.

II. THEORETICAL MODEL

Figure 1(a) shows a sketch of the APT and the IR laser electric fields. We assume an IR electric field pulse with a $\sin^2$ envelope, pulse length $\tau_{\rm IR}$, and frequency $\omega/(2\pi)$,

$$E(t) = E_0 \sin^2[\pi(t-\Delta t)/\tau_{\rm IR}]\sin[\omega(t-\Delta t)], \quad t-\Delta t \in [0,\tau_{\rm IR}]. \tag{1}$$

The field amplitude E_0 in atomic units is related to the intensity I in units of W/cm^2 by $E_0 = \sqrt{I/I_0}$ with $I_0 = 3.51 \times 10^{16}$ W/cm^2. We define the time delay Δt as the offset between the centers of the APT and the IR pulse and assume Δt to be positive if the center of the APT precedes the center of the IR pulse.

Attosecond XUV pulses are generated by first ionizing a (usually) atomic target in the IR field in such a way that the released electron accumulates energy from the IR laser electric field. This energy is released in the form of HHs upon the electron's recollision with the target [4–7]. In the most common experimental setup [24,25], these recollisions occur twice per IR period $T_{\rm IR}$, such that the APT consists of XUV pulses that are equally separated by $\delta t = T_{\rm IR}/2$. Each attosecond pulse in the train ionizes the neutral molecule and creates a nuclear wave packet in H_2^+. Even without the presence of an IR laser pulse, this wave packet evolves, spreads, and dephases in the $1s\,\sigma_g$ adiabatic electronic potential curve, as shown in Figs. 1(b), 2(b), and 2(c). Half an IR period later, the next H_2^+ wave packet is born and behaves the same way. The time-delayed IR laser field couples the $1s\,\sigma_g$ and $2p\,\sigma_u$ potentials curves, producing IR-field-dressed potential curves along which H_2^+ may dissociate via bond softening (BS) [23,26,27] and, possibly, bond hardening [23,28].

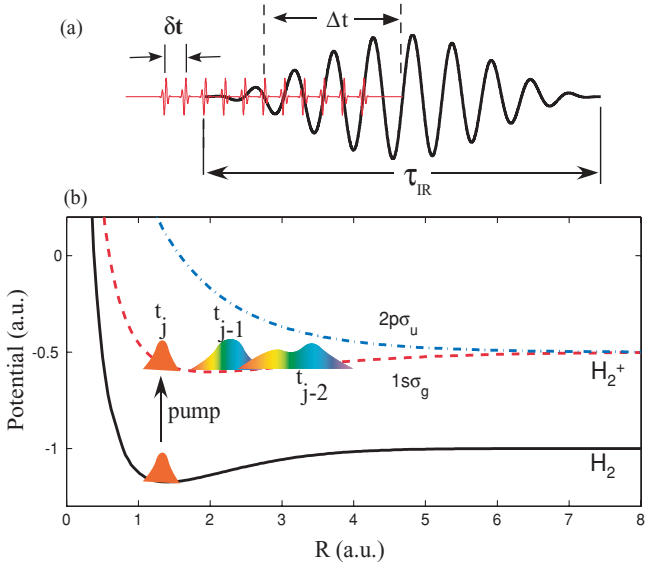

FIG. 1. (Color online) (a) Schematic of the APT and IR laser field. The time delay Δt is the offset between the centers of the APT and IR pulses. The pulse duration of the IR pulse is $\tau_{\rm IR}$ and the separation between subsequent attosecond pulses is δt. (b) The relevant Born-Oppenheimer potential curves of H_2 and H_2^+. A sequence of H_2^+ nuclear vibrational wave packets is generated on the $1s\,\sigma_g$ electronic ground-state potential curve of H_2^+ by repeated ionization of H_2 in subsequent XUV pulses of the APT.

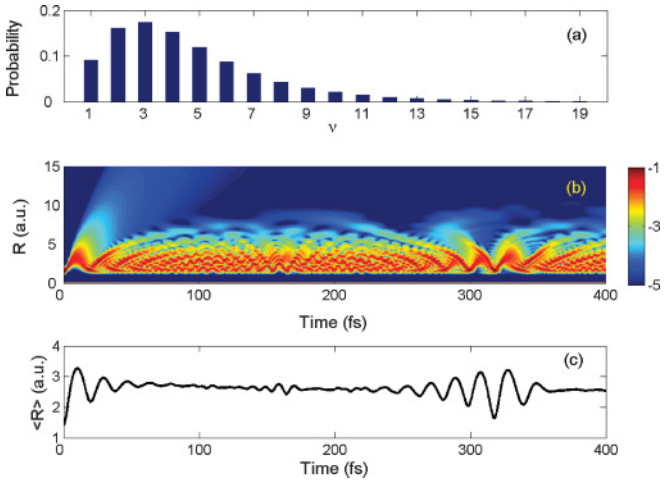

FIG. 2. (Color online) (a) FC distribution for the 19 bound vibrational states of the H_2^+ electronic ground state. (b) Probability density (logarithmic color scale) for the field-free evolution of the wave packet in the $1s\,\sigma_g$ potential curve of H_2^+. The wave packet is launched at time $t = 0$ by an FC transition from the (vibrational) ground state of H_2. (c) Corresponding expectation value of the internuclear distance as a function of time.

For simplicity, we assume that all attosecond pulses in the APT have the same amplitude, which is supposed to be sufficiently low such that depletion of H_2 can be neglected. Thus, each attosecond pulse is assumed to create, with the same probability, delayed replicas of a nuclear vibrational wave packet in H_2^+. The exposure of H_2 to the APT then generates a coherent superposition of electronic-nuclear wave packets:

$$\Phi(r_1,r_2,R;t) = \phi_{\rm H_2}(r_1,r_2,R;t) + \sum_j \mathbb{S}\left[\phi_{\rm H_2^+}(r_1,R;t,t_j)\varphi(r_2;t,t_j)\right], \tag{2}$$

where $\phi_{\rm H_2}(r_1,r_2,R;t)$ is the wave function of the remaining neutral molecule, and R is the internuclear distance. The index j marks the jth attosecond pulse in the train. $\phi_{H_2^+}(R,r;t,t_j)$ designates the vibrationally excited molecular ion that is generated by an XUV pulse in the APT at time t_j, accompanied by and phase coherent with the wave packet $\varphi(r;t,t_j)$ of the released electron. Since initially the neutral molecule is in a singlet spin state and no spin-dependent interactions are included, antisymmetrization of the total (two electron plus two nuclei) molecular wave function requests its spatial

part to remain symmetrized at all times. This is guaranteed by the symmetrization operator $\mathbb{S}$. As this work focusses on coherence effects between successively launched nuclear H_2^+ wave packets, we adopt an easy-to-handle model for the primary ionization processes, describing the launch of individual nuclear wave packets in the Franck-Condon (FC) approximation. This approximation is physically appropriate in our context and implies the instant (on the time scale of the nuclear motion) removal of one molecular electron by an attosecond XUV pulse. This sudden ionization results in (i) a nuclear wave packet in H_2^+ that does not dependent on characteristics of the pump pulse (such as intensity and carrier frequency) and (ii) a photoelectron wave packet φ as the main recipient of the very broad (several eV wide) spectral profile of the attosecond XUV pump pulse. In contrast to molecular ionization in long (thus spectrally sharp) pulses [29], the asymptotic energy of the emitted photoelectron is not linked to a particular ro-vibrational state of the residual molecular ion.

From (2), we obtain the nuclear probability density in H_2^+ by integration over the electronic coordinates,

$$\begin{aligned}\rho(R,t) &= \int\int dr_1 dr_2 \left| \sum_j \mathbb{S}[\phi_{H_2^+}(r_1,R;t,t_j)\varphi(r_2;t,t_j)] \right|^2 \\ &= \sum_j \int dr |\phi_{H_2^+}(r,R;t,t_j)|^2 \\ &\quad + \sum_{i\neq j} f_{i,j}(t) \int dr \phi^*_{H_2^+}(r,R;t,t_i)\phi_{H_2^+}(r,R;t,t_j) \\ &\quad + \sum_{i,j} g_{i,j}(t) g_{j,i}(t)^*, \end{aligned} \tag{3}$$

with the definitions of "exchange" and "direct" integrals

$$g_{i,j}(t) = \int dr \phi^*_{H_2^+}(r,R,t,t_i)\varphi(r,t,t_j), \tag{4}$$

$$f_{i,j}(t) = \int dr \varphi^*(r;t,t_i)\varphi(r;t,t_j), \tag{5}$$

respectively. The integrals $g_{i,j}$ arise from the exchange symmetry of the two electrons. Assuming (in the FC approximation) rapid emission of electron wave packets, we neglect all products $g_{ij}g^*_{ji}$ of exchange integrals in our numerical simulations.

The overlap of emitted photoelectron wave packets f_{ij} parameterizes the degree of coherence in the accumulation of nuclear wave packets generated by the APT. For odd differences $i-j$, the phases of the ith and jth attosecond pulse differ by π (modulo 2π), corresponding to the emission of electron wave packets $\varphi(r;t,t_i)$ and $\varphi(r;t,t_j)$ in opposite directions [30]. In this case, we neglect the overlap between these two electron wave packets by setting $f_{i,j}(t)=0$, thereby suppressing interference between the corresponding two nuclear wave packets. On the other hand, for even differences $i-j$, we include the overlap between electron wave packets that are emitted by XUV pulses that pull the photoelectron in the same direction at times separated by integer multiples of T_{IR}. Within this model, we consider the two following limiting cases in our numerical calculations: (i) in the limit of maximal coherence between separately launched nuclear wave packets, we assume that $|f_{i,j}|=1$ if $i-j$ is even and $|f_{i,j}|=0$ for odd $i-j$. (ii) In the opposite extreme case, we completely eliminate all interferences between individual nuclear wave packets by setting $|f_{i,j}|=0$ for all i,j. This amounts to only including the incoherent superposition of successively launched nuclear wave packets as given by the term $\sum_j \int dr |\phi_{H_2^+}(r,R;t,t_j)|^2$ in (3).

In order to account for the evolution of the nuclear motion in H_2^+, we neglect molecular rotation [15] and represent the vibrational dynamics on the two lowest Born-Oppenheimer (BO) potential curves [cf. Fig. 1(b)],

$$\phi_{H_2^+}(r,R;t,t_j) = \sum_{k=g,u} \chi_k(R,t,t_j)\varphi_{H_2^+,k}(r;R), \tag{6}$$

where $\varphi_{H_2^+,k}$ designates the adiabatic electronic wave functions of H_2^+ in the $1s\ \sigma_g$ electronic ground state (index g) and $2p\ \sigma_u$ first excited state (index u). The nuclear dynamics initiated by a SAP at time t_j is calculated by solving the two-state time-dependent Schrödinger equation

$$\begin{aligned} i\frac{\partial}{\partial t}\begin{pmatrix}\chi_g(R;t,t_j)\\ \chi_u(R;t,t_j)\end{pmatrix} \\ = \begin{pmatrix} T_R+V_g(R) & D_{gu} \\ D_{gu} & T_R+V_u(R)\end{pmatrix}\begin{pmatrix}\chi_g(R;t,t_j)\\ \chi_u(R;t,t_j)\end{pmatrix}. \end{aligned} \tag{7}$$

Using the FC approximation, we start the propagation with the unoccupied initial ungerade state $\chi_u(R,t=t_j,t_j)=0$ and set the initial gerade state $\chi_g(R,t=t_j,t_j)$ equal to the vibrational ground state $\chi_{H_2}(R;t=t_j)$ in the electronic ground state of H_2. The elements of the Hamiltonian matrix are given by the BO potential curves $V_{g/u}(R)$ of the $1s\ \sigma_g$ and $2p\ \sigma_u$ electronic states [31], the nuclear kinetic energy operator $T_R=-(M^{-1})\partial^2/\partial R^2$, the mass M of the proton, the coupling matrix elements $D_{gu}(R,t)=E(t)d_{gu}(R)$, and the dipole transition amplitudes $d_{gu}(R)$ [32]. For the incoherent case (all $f_{i,j}=0$), we independently evolve the nuclear wave functions $\{\chi_{g/u}(R;t,t_j)\}$ that are generated by individual SAPs of the pulse train at times $\{t_j\}$ and add their probabilities at the end of the simulation. In contrast, for maximal coherence ($f_{i,j}=1$ for even $i-j$), we feed successive nuclear wave packets into the $1s\ \sigma_g$ curve of H_2^+ and keep track of the phase accumulation in the neutral molecule prior to its (partial) ionization at times $\{t_j\}$,

$$\chi_g(R,t=t_j,t_j) = \chi_{H_2}(R,t=0)\exp[-i\theta(t_j)]. \tag{8}$$

Up to an irrelevant overall phase, the accumulated phase at time t_j is given by

$$\theta(t_j) = (\xi_{H_2} - \langle E_{H_2^+}\rangle)t_j + j\pi, \tag{9}$$

where ξ_{H_2} is the ground state energy of H_2 and

$$\begin{aligned}\langle E_{H_2^+}\rangle &= \langle\chi_{H_2}(R;t_j)| -\frac{1}{M}\frac{\partial^2}{\partial R^2} + V_g(R)|\chi_{H_2}(R;t_j)\rangle \\ &= -0.565 \end{aligned} \tag{10}$$

is the average energy of the nuclear wave packet in the $1s\ \sigma_g$ potential surface of H_2^+. The first term in (9) accounts for the phase accumulation in the neutral molecule. With the second phase contribution in (9), $j\pi$, we represent the ATP as a sequence of ultrashort electric field spikes with alternating

electric field directions. We assume that electrons released in the same direction by different SAPs in the APT all carry off the same phase, which is consistent with the assumption of $f_{i,j} = 1$ for all even $i - j$.

After the IR laser pulse has passed, we continue to freely propagate (7) for a sufficiently long time (100 fs) to allow the nuclear wave packet to completely enter the interval $R > 20$. This enables us to separate its bound part from its dissociating part $\chi^+_{g/u}(R,t)$. In order to determine the proton energy spectrum, we Fourier transform the dissociating parts of the nuclear wave packet over the interval $R \in [20,120]$ to obtain the momentum representations,

$$\tilde{\chi}^+_{g/u}(P,t) = \int_{20}^{120} dR\ \chi^+_{g/u}(R,t)\exp(-iPR). \quad (11)$$

The distribution of proton-fragment energies $K = P^2/(8M)$ as a function of the delay is now obtained as

$$S(K,\Delta t) = 4M[|\tilde{\chi}^+_g(P;\Delta t)|^2 + |\tilde{\chi}^+_u(P;\Delta t)|^2]/P. \quad (12)$$

Note that K equals one half of the total KER of the proton and hydrogen atom fragments.

Quantum-beat spectroscopy [22] offers a tool to analyze the dynamics of laser-molecule interactions with regard to the significance of the stationary ro-vibrational state distribution in a ro-vibrational wave packet. This method was recently applied to hydrogen molecular ions to image molecular vibrational potential curves [21,22], analyze ro-vibrational couplings [15], and to characterize dissociation mechanisms [23]. In the context of the present work, we analyze quantum-beat spectra to correlate vibrational levels in the molecular ion to specific the proton energies K. Removing the delay-independent components in $S(K,\Delta t)$ [22] and Fourier transforming the remaining delay-dependent proton energy-release spectrum $S_{\rm dyn}(K,\Delta t)$ results in the power spectrum

$$\tilde{S}(K,f) = \left|\int_0^{\Delta t_{\rm max}} d\Delta t\ S_{\rm dyn}(K,\Delta t)\exp(-i2\pi f\Delta t)\right|, \quad (13)$$

where a sampling time $\Delta t_{\rm max} > 1$ ps allows for the resolution of all relevant vibrational beat frequencies.

III. NUMERICAL RESULTS

A. Single attosecond pulse

Within our model, when exposed to an SAP, the neutral H_2 molecule absorbs one XUV photon, emits one electron, and leads to the formation of a molecular ion H_2^+ in a coherent superposition of bound and continuous nuclear states in the $1s\ \sigma_g$ adiabatic electronic state. Within the FC approximation, the probability distribution in the 19 bound vibrational states of the H_2^+ electronic ground state is shown in Fig. 2(a). The corresponding cumulative contribution of all FC overlaps with unbound nuclear states of the H_2^+ electronic ground state amounts to about 1.3% and gives rise to a small contribution of direct dissociation in the SAP (and in each XUV pulse of an APT, see below). The subsequent free evolution of this vibrational wave packet has been studied before, both theoretically [19] and experimentally [20]. Apart from direct dissociation in the SAP, the bound vibrational motion in H_2^+ is characterized by alternating intervals of dephasing and revivals, as shown in Fig. 2(b) for its probability density $|\chi^+_g(R,t)|^2$ and in Fig. 2(c) for the expectation value $\langle R(t)\rangle = \langle\chi^+_g(R,t)|R|\chi^+_g(R,t)\rangle$ of the molecular ion's internuclear distance. Without the laser field, the vibrational wave packet oscillates in the potential well of $1s\ \sigma_g$ adiabatic potential about an average internuclear distance of approximately 2.6 with a vibrational period of about 25 fs. The wave packet dephases after about three vibrational periods. It then experiences quarter and half revivals at about 160 fs and 320 fs after its launch.

B. Single attosecond and IR pulse

By adding a time-delayed IR pulse, H_2^+ can dissociate into a proton and hydrogen atom, generating a fragment energy distribution that depends on the laser parameters. Previous calculations [33–35] and recent measurements [36,37] found a pronounced dependence of the dissociation asymmetry (i.e., of the final localization of the electron near one of the separating nuclei, on the time-delay Δt). This indicates that the subcycle evolution of the IR electric field plays a crucial role in the dissociation of the molecular ions. This was confirmed in a recent experiment with single phase-stabilized pulses [38].

For an SAP, the coherent terms in (3) are absent. If the IR pulse length $\tau_{\rm IR}$ is shorter than the nuclear vibration period, the IR pulse can be used to resolve in time the internuclear motion by mapping it onto the delay-dependent proton energy spectrum $S(K,\Delta t)$, as shown for a pulse with $\tau_{\rm IR} = 5\ T_{\rm IR}$ in Fig. 3(a). Protons emitted with kinetic energies below 0.2 eV are due to direct dissociation in the SAP. They are not noticeably influenced by the IR laser field and therefore not sensitive to the time delay. The power spectrum $\tilde{S}(K,f)$ is displayed in Fig. 3(b). The total dissociation yields are obtained by integrating the results in Fig. 3(a) over

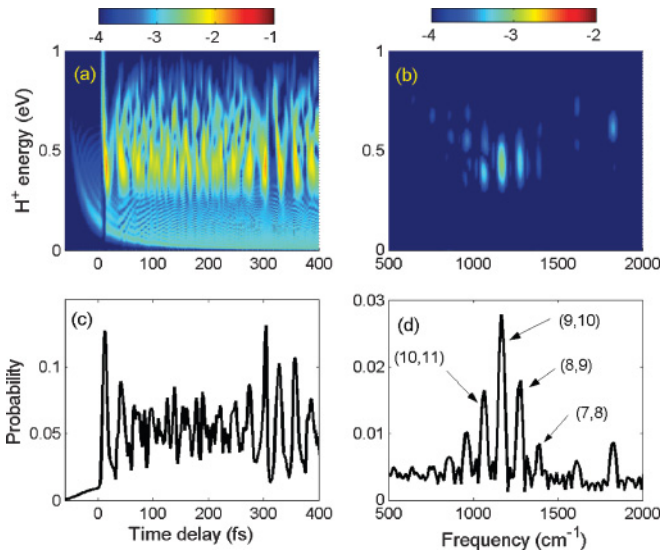

FIG. 3. (Color online) (a) Time-dependent proton energy distribution for a SAP and a delayed 10^{13} W/cm^2, 800 nm, $\tau_{\rm IR} = 5T_{\rm IR}$ IR laser pulse. (b) Corresponding power spectrum as a function of the proton energy and beat frequency. Panels (c) and (d) are the dissociation yields obtained by integration of (a) and (b) over the energy distribution, respectively.

all energies as a function of the SAP-IR delay [Fig. 3(c)]. Note that Figs. 3(b) and 3(d) do not include the large zero-frequency contribution of $S(K,\Delta t)$ [22] and show the relative contribution of quantum beats. The peak intensity of the IR pulse in this simulation is 10^{13} W/cm^2.

Figure 3(a) shows some similarity with Fig. 2(b) with regard to the display of the oscillating vibrational motion and the two first (quarter and half) revivals. Initially, and near the revivals, the dissociation probability oscillates with the time delay between the SAP and IR pulses, resembling the motion of a classical oscillator. In these time intervals, the dissociation probability shows distinct maxima when the well-localized nuclear wave packet approaches the outer classical turning point [Fig. 3(c)]. The most prominent frequencies f in the power spectrum $\tilde{S}(K,f)$ in Fig. 3(d) correspond to quantum beats $\Delta\nu = \nu' - \nu$ between the vibrational states $(\nu,\nu') = (8,9)$, $(9,10)$, and $(10,11)$, indicating that the largest contributions to the dissociation originate in the vibrational states $\nu = 8-11$ of the $1s\,\sigma_g$ BO electronic state of H_2^+. Fragments from these states escape with kinetic energies near 0.5 eV. Smaller quantum-beat frequencies below 1000 cm^{-1} correspond mainly to higher proton energies and involve higher vibrational states. Figures 3(b) and 3(d) also show faint lines at ~1600 and ~1800 cm^{-1} that are due to vibrational quantum beats with $\Delta\nu = 2$.

The combination of a SAP and a longer IR pulse leads to a radically changed energy spectrum. Figure 4 shows the same simulation as Fig. 3, but for a $\sin^2$ IR pulse of total length $\tau_{IR} = 30T_{IR}$. In this case, the nuclear wave packet approaches the outer turning point twice during τ_{IR}, and dissociation mainly occurs at two distinct times. The corresponding fragments are coherently generated at different times and interfere, causing the complex interference structure in the energy dependence of the delay-dependent spectrum in Fig. 4(a). This interference tends to decrease the oscillation amplitude of the dissociation yield as a function of Δt. Indeed, in the average over the displayed delay interval, the total dissociation probability in Fig. 4(c) oscillates with a smaller amplitude compared with that in Fig. 3(c). Note, in particular, that the large oscillation-amplitude enhancement near the wave-packet revival at $\Delta t \sim 320$ fs for the 5-IR-cycle pulse in Fig. 3(c) is absent for the 30-IR-cycle pulse in Fig. 4(c). As expected, the total dissociation probability in Fig. 4(c) tends to be larger than for the short IR pulse in Fig. 3(c). Note also that the power spectrum for the 30-IR-cycle pulse in Fig. 4(d) is dominated by just two beat frequencies corresponding to $(\nu,\nu') = (7,8)$ and $(8,9)$, whereas for the 5-IR-cycle pulse in Fig. 3(d), more vibrational frequencies contribute, thus generating the more complicated temporal structure in the 5-IR-cycle results in Fig. 3(c).

If the IR pulse duration τ_{IR} is much longer than the vibrational period, the time-dependent proton energy distribution and corresponding power spectra change significantly in comparison with our results for $\tau_{IR} = 5\ T_{IR}$ in Fig. 3 and $\tau_{IR} = 30T_{IR}$ in Fig. 4. As an example, we show such long-pulse results in Fig. 5 for $\tau_{IR} = 70T_{IR}$ with all other parameters as in Figs. 3 and 4. Within this long IR pulse, we can clearly identify for any value of Δt four "dissociation jets" in the evolving nuclear distribution $\rho(R,\Delta t)$ in (3) (not shown), corresponding to four successive approaches of the nuclear wave packet to the bond-softening region on the IR field-dressed lowest H_2^+ BO potential curve. These dissociating wave packets interfere, leading to distinct interference maxima along the proton energy axis in Fig. 5(a) for delays outside the overlap region between the two pulses.

In contrast to the results in Fig. 3 for which the spectral bandwidth of the short IR pulse (~100 meV) is wide enough to blur the energy difference between different vibrational states (~100 meV = 807 cm^{-1}), for $\tau_{IR} = 70T_{IR}$ the corresponding narrow bandwidth allows for the resolution of vibrational state contributions in the dissociating wave packets in terms of distinct proton energies. The dominant part in the power spectrum in Fig. 5(d) shows that almost all fragments originate in the $\nu = 7$ and 8 vibrational states. In contrast to the results in Figs. 3(b), 3(d), 4(b), and 4(d) relative contributions from the $\nu \geqslant 9$ states are very small. For nonoverlapping SAP and IR

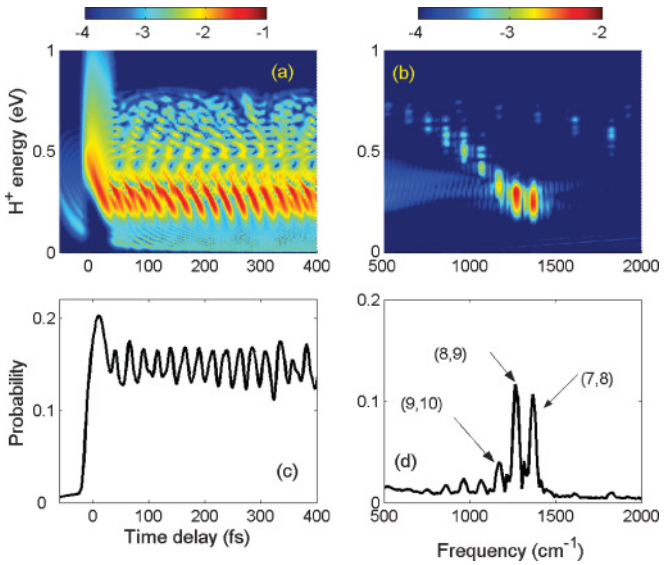

FIG. 4. (Color online) Same as Fig. 3, but for an IR pulse length of $\tau_{IR} = 30T_{IR}$.

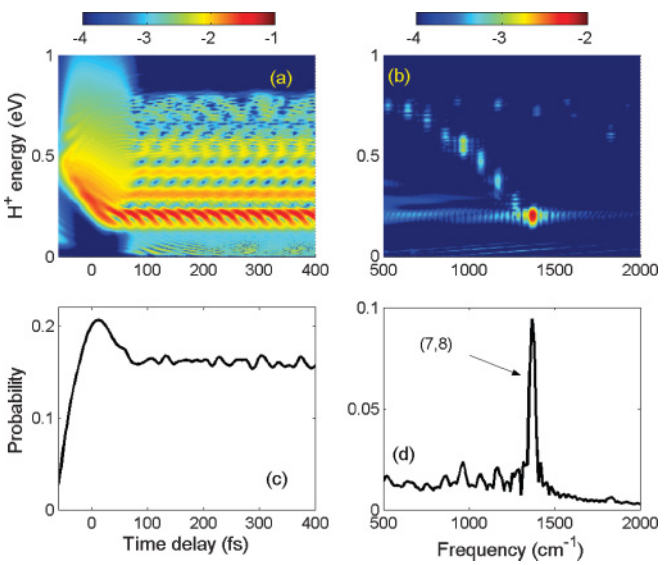

FIG. 5. (Color online) Same as Figs. 3 and 4, but for an IR pulse length of $\tau_{IR} = 70T_{IR}$.

pulses (i.e., for $\Delta t > 35T_{IR}$), dissociation leads to proton energies in distinct, relatively narrow energy intervals [Fig. 5(a)], but no pronounced oscillation in the total dissociation probability [Fig. 5(c)] as a function of Δt. The maximum dissociation probabilities in Figs. 4 and 5 are almost the same, which means that both the $\tau_{IR} = 30T_{IR}$ and $\tau_{IR} = 70T_{IR}$ IR pulses almost fully deplete the $\nu = 7$, 8, and 9 vibrational states. The maximum dissociation yields in Figs. 4(c) and 5(c) appear at $\Delta t = 11$ and 13 fs, respectively, since the nuclear wave packets reach the outer turning point near the peak of the IR-pulse envelope. In contrast, at larger delays and for nonoverlapping SAP and IR pulses, the dissociation yield is smaller (in part) due to dephasing of the vibrational wave packet in the leading half of the IR pulse.

The dependence of the proton energy distribution on the intensity of the IR pulse is shown in Fig. 6 for a fixed pulse duration of $\tau_{IR} = 30T_{IR}$ and peak intensities of 3×10^{12} W/cm^2 (upper row), 7×10^{12} W/cm^2 (middle row), and 2×10^{13} W/cm^2 (lower row). The figure shows the emitted proton energy distribution as a function of time delay (left column) and beat frequency (right column). For increasing laser intensity, the most likely proton energy is shifted to lower energies, while the overall dissociation yield increases with intensity, as expected. The power spectra (right column) illustrate the reason for this shift in fragment energies: as the peak intensity increases, the main contributions to the dissociation yield originate in lower vibrational states, due to progressive bond softening [23]. The main contributors at the lowest intensity, 3×10^{12} W/cm^2, are vibrational states with $\nu = 8$, 9, and 10 compared to $\nu = 7$, 8, and 9 at 7×10^{12} W/cm^2. At the highest intensity, 2×10^{13} W/cm^2, this shift proceeds to $\nu = 6$, 7, 8, and 9.

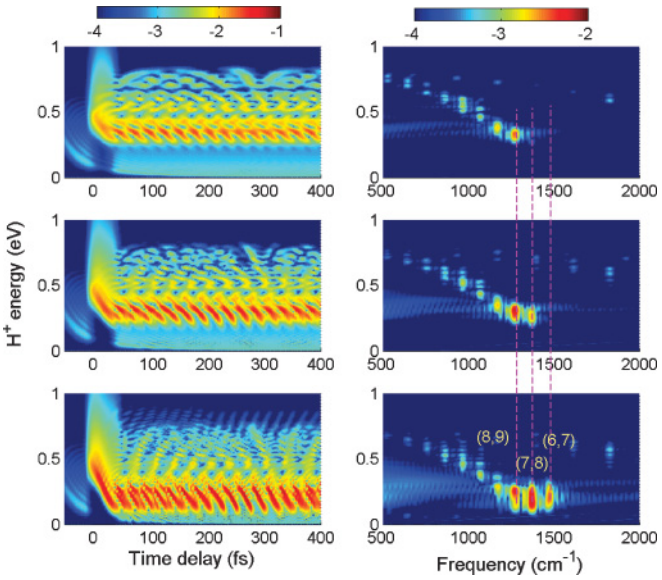

FIG. 6. (Color online) Time-dependent proton-energy distribution (left column) and power spectrum (right column) for an SAP and a delayed IR laser pulse with a pulse length of 30-IR cycles and peak laser intensities of 3×10^{12} W/cm^2 (upper row), 7×10^{12} W/cm^2 (middle row), and 2×10^{13} W/cm^2 (lower row). The vertical dashed lines in the right column guide the eye in comparing quantum beats at different intensities.

C. APT and IR laser fields

Exposure of neutral H_2 molecules to an APT results in the generation of a sequence of photoelectron wave packets that are entangled with nuclear vibrational wave packets in H_2^+. Wave packets launched by different XUV pulses of the APT are coherent and interfere. Such an effect was recently demonstrated experimentally by observing the interference between photoelectron wave packets emitted in successive half cycles of a phase-stabilized few-cycle IR pulse [39]. Recall that, according to (3), the interference of H_2^+ nuclear wave packets depends on the overlap $f_{i,j}$ between electron wave packets launched by different attosecond pulses in the train.

To examine the relevance of such coherence effects on the delay-dependent proton energy distribution, we next examine the limiting cases of incoherent superpositions of individual H_2^+ nuclear wave packets ($f_{i,j} = 0$) and full coherence. For the fully coherent case with $f_{i,j} = 1$ for even $i - j$ and $f_{i,j} = 0$ for odd $i - j$, we first coherently propagate only the nuclear wave packets initiated at times $t_{j=2n+1}$, where n is an integer. These XUV ionization times are separated by T_{IR}. As a result, we find the contributions $S(K,\Delta t)^{odd}$ and $\tilde{S}(K,f)^{odd}$ to the delay-dependent KER and frequency-dependent power spectrum, respectively. Similarly, by only propagating the coherent superposition of nuclear wave packets initiated at $t_{j=2n}$, we obtain $S(K,\Delta t)^{even}$ and $\tilde{S}(K,f)^{even}$. Finally, we add the even and odd contributions in the coherent KER and power spectra,

$$S(K,\Delta t) = S(K,\Delta t)^{even} + S(K,\Delta t)^{odd}, \quad (14)$$

$$\tilde{S}(K,f) = \tilde{S}(K,f)^{even} + \tilde{S}(K,f)^{odd}. \quad (15)$$

Nuclear wave packets born at times t_j evolve on the laser dressed $1s\ \sigma_g$ and $2p\ \sigma_u$ BO potential curves with starting phases $\theta(t_j)$ given in (9). Since $\theta(t_j)$ sensitively depends on T_{IR}, interference effects in the proton energy spectrum will respond critically to small changes in the carrier wavelength of the IR pulse. This is illustrated in Fig. 7 for $\delta t = 55$ (upper row, corresponding to an IR carrier wavelength of $\lambda_{IR} = 800$ nm) and $\delta t = 50$ (lower row, corresponding to $\lambda_{IR} = 727$ nm). For both wavelengths we used a 30-IR-cycle pulse and modeled the APT in terms of 14 alternating electric field attosecond pulses (using the FC approximation). The interference structures in the time-dependent proton energy distribution (left column) and corresponding power spectrum (right column) strongly deviate for the two carrier wavelengths, despite the small wavelength difference, since the corresponding small difference in δt induces a significant shift in the starting phases of consecutively launched H_2^+ nuclear wave packets. The interference between different H_2^+ wave packets strongly influences the proton energy spectrum, and the total dissociation probabilities vary over one order of magnitude for these two values of δt. In addition, the power spectra reveal contributions to the total dissociation yield that derive from different vibrational states, strongly depending on λ_{IR}, as changes in θ_{t_j} affect the overall shape of the composite emitted nuclear wave packet.

Interestingly, for overlapping APT and IR laser pulses (i.e., for delays below ~50 fs), the continuum of nuclear states—generated into the dissociating part of the $1s\ \sigma_g$ BO potential curve in the molecular ion by XUV ionization of the neutral

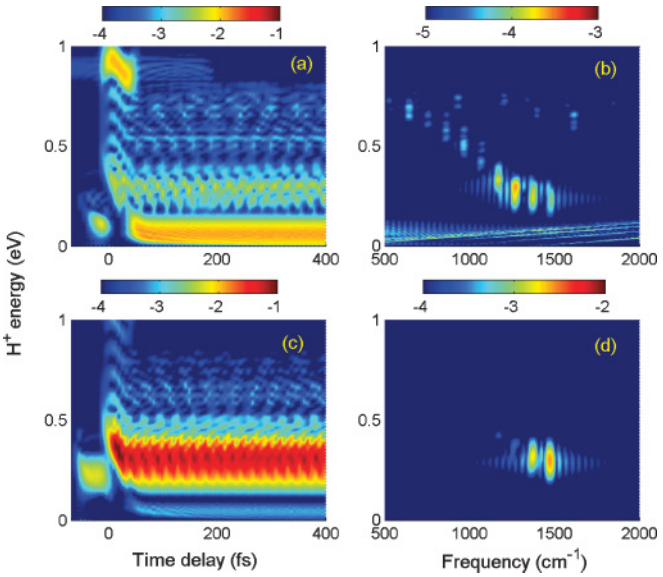

FIG. 7. (Color online) Time-dependent proton energy distributions (left column) and corresponding power spectra (right column) for H_2 exposed to an APT and a delayed 30-cycle IR laser pulse with a peak intensity of 10^{13} W/cm^2. The APT consists of 14 alternating attosecond XUV pulses. Maximal coherence (see text) is assumed for the superposition of individual H_2^+ nuclear wave packets. Panels (a) and (b) show results for an IR carrier wavelength of $\lambda_{IR} =$ 800 nm. Panels (c) and (d) show results for $\lambda_{IR} = 727$ nm.

molecule—is excited in the IR pulse to the antibonding $2p\,\sigma_u$ state of the ion. This leads to a strong coherent accumulation of relatively energetic fragments near 1 eV [Fig. 7(a)]. In contrast, for delays at which the APT and IR pulse do not overlap, states in the vibrational continuum of the $1s\,\sigma_g$ potential curve dissociate without further excitation and, in consequence, gain much lower KERs of $\lesssim$0.1 eV. The same two dissociation channels are also visible at a different IR wavelength (727 nm) in Fig. 7(c). However, they are much less prominent due to a more destructive accumulation of nuclear-wave-packet contributions.

For the fully incoherent superposition of individual H_2^+ nuclear wave packets ($f_{i,j} = 0$), the total time-dependent proton energy distribution is simply given by adding the individual proton energy distributions,

$$S_{\rm inc}(K,\Delta t) = \sum_j S(K,\Delta t, t_j). \tag{16}$$

The results of a simulation for a 30-IR-cycle pulse and an APT with 2 [Fig. 8(a)], 11 [Fig. 8(b)], and 20 [Fig. 8(c)] attosecond pulses, show that the time-dependent structure in the proton energy spectra becomes less prominent as the number of individual XUV pulses is increased.

Our numerical results for the fully incoherent superposition of 20 H_2^+ nuclear wave packets in Fig. 8(c) are in qualitative agreement with the experimental proton energy distribution for 35 fs FWHM IR pulses in Fig. 1(b) of reference [18]. As in our Fig. 8(c), the experiment shows no significant time-dependence of the proton energy distribution outside

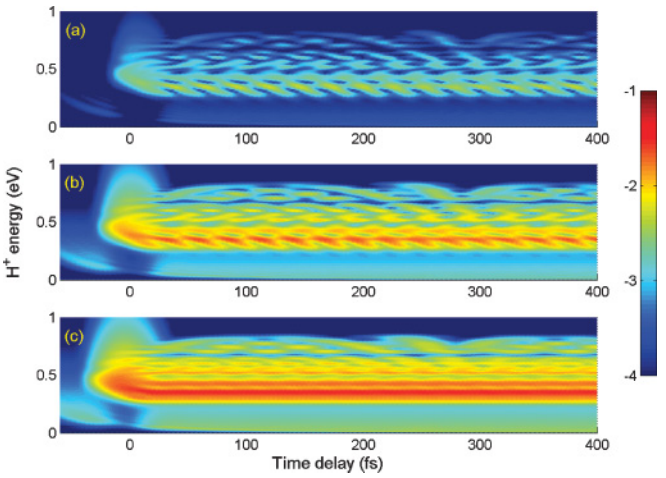

FIG. 8. (Color online) Time-dependent proton kinetic energy distribution for the incoherent superposition of H_2^+ nuclear vibrational wave packets launched by an ATP with (a) 2-, (b) 11-, and (c) 20-attosecond pulses. The IR pulse duration is $30T_{IR}$ and the laser intensity is 3×10^{12} W/cm^2.

the temporal overlap of ATP and IR pulse and displays no (obvious) interference effects.

IV. SUMMARY AND OUTLOOK

We studied the dissociative ionization of H_2 in an SAP or APT and a time-delayed IR laser pulse. For an SAP and IR pulse, we analyzed the time-dependent proton energy spectra for different IR pulse durations and laser intensities and described how a time-delayed ultrashort IR pulse maps the nuclear motion in H_2^+. By simultaneously examining the power spectra of the proton energy distribution, we identified vibrational state components of the nuclear wave packets with the largest contributions to the proton energy spectra and total dissociation yields. For APTs and delayed IR pulses, we examined how the interference between H_2^+ wave packets that are launched by different attosecond pulses of the APT imprints time- and energy-dependent interference structures on the proton energy distribution.

In order to keep the computational effort at a manageable level, we introduced simplifying approximations. Focussing on inference effects that are due to the sequential generation of nuclear wave packets in H_2^+ by successive XUV pulses in an attosecond pump-pulse train, we modeled the launch of individual nuclear wave packets in FC approximation. Furthermore, consistent with the underlying physical assumption in the FC approximation of rapid ionization of the neutral molecule by any XUV pulse in the APT, we neglected the overlap between rapidly escaping photoelectrons and the residual molecular ion. While these approximations will, to some extent, affect the coherence between separately launched nuclear wave packets, we believe that our model includes the most important aspects of the nuclear wave packet coherence. Within this model, we then examined two limiting cases. First, assuming maximal overlap between photoelectron wave packets that are successively emitted in the APT in the same direction [30], we found strong interference effects in the delay

and fragment-energy dependence of KER spectra. Second, for the other extreme case of no coherence between successively generated nuclear wave packets, we find that the KER spectra become much less structured than for the coherent case, in agreement with recent experimental results [18].

In the absence of a firm lower limit for the effects of nuclear wave packet interferences on the KER, it would be premature to view our numerical examples as a proof for the absence of nuclear wave packet interferences in the experiments by Kelkensberg *et al.* [18]. Our numerical results tend to overestimate the correlation between photoelectron wave packets that are emitted by different XUV pulses in the APT on nuclear wave packet interferences and thus may be regarded as an upper limit for the manifestation of such interference effects in KER spectra. However, these results provide evidence for the necessity of observing in coincidence heavy fragments and photoelectrons for the appearance of the discussed APT-induced interference effects in measured KER spectra. In contrast, not observing the emitted electron in coincidence with the proton fragments amounts to randomizing the phases of individual nuclear wave packets and hence to their detection in the form of an incoherent superposition. We note that this interpretation is in conflict with the model calculations in [18] that are based on a coherent superposition of contributions to the KER from individual attosecond pulses.

For the future, we anticipate refined experiments in which protons and XUV-pulse-emitted electrons are detected in coincidence. Assuming that such experiments can be carried out with sufficiently large count rates, we predict an interesting transition from an incoherent to a coherent superposition of nuclear wave packets as photoelectrons are recorded in increasingly narrower momentum bins. For the coherent proton KER spectra, we find an extremely sensitive dependence on the IR wavelength, which might be exploited to characterize the IR laser pulse in terms of interference effects (in both delay and proton energy) in fragment KER spectra. With regard to future numerical simulations, we note that—even for the simplest molecule H_2—more work is needed in order to establish a firm lower limit for the effect of nuclear wave packet interferences on KER spectra.

ACKNOWLEDGMENTS

This work is supported by the Division of Chemical Sciences, Office of Basic Energy Sciences, Office of Energy Research of the US Department of Energy and by the NSF.

[1] A. Scrinzi, M. Yu. Ivanov, R. Kienberger, and D. M. Villeneuve, J. Phys. B **39**, R1 (2006).
[2] F. Krausz and M. Yu. Ivanov, Rev. Mod. Phys. **81**, 163 (2009).
[3] A. L. Cavalieri, N. Müller, Th. Uphues, V. S. Yakovlev, A. Baltuska, B. Horvath, B. Schmidt, L. Blümel, R. Holzwarth, S. Hendel, M. Drescher, U. Kleineberg, P. M. Echenique, R. Kienberger, F. Krausz, and U. Heinzmann, Nature (London) **449**, 1029 (2007).
[4] J. L. Krause, K. J. Schafer, and K. C. Kuler, Phys. Rev. Lett. **68**, 3535 (1992).
[5] C. G. Wahlström, J. Larsson, A. Persson, T. Starczewski, S. Svanberg, P. Salières, P. Balcou, and A. L'Huillier, Phys. Rev. A **48**, 4709 (1993).
[6] P. B. Corkum, Phys. Rev. Lett. **71**, 1994 (1993).
[7] M. Lewenstein, Ph. Balcou, M. Yu. Ivanov, A. L'Huillier, and P. B. Corkum, Phys. Rev. A **49**, 2117 (1994).
[8] P. Agostini and L. F. DiMauro, Rep. Prog. Phys. **67**, 813 (2004).
[9] P. B. Corkum and F. Krausz, Nature Phys. **3**, 381 (2007).
[10] M. B. Gaarde, J. L. Tate, and K. J. Schafer, J. Phys. B **41**, 132001 (2008).
[11] M. Drescher, M. Hentschel, R. Kienberger, M. Uiberacker, V. Yakovlev, A. Scrinzi, T. Westerwalbesloh, U. Kleineberg, U. Heinzmann, and F. Krausz, Nature (London) **419**, 803 (2002).
[12] M. Uiberacker, T. Uphues, M. Schultze, A. J. Verhoef, V. Yakovlev, M. F. Kling, J. Rauschenberger, N. M. Kabachnik, H. Schröder, M. Lezius, K. L. Kompa, H. G. Muller, M. J. J. Vrakking, S. Hendel, U. Kleineberg, U. Heinzmann, M. Drescher, and F. Krausz, Nature (London) **446**, 627 (2007).
[13] E. Goulielmakis, M. Uiberacker, R. Kienberger, A. Baltuska, V. Yakovlev, A. Scrinzi, T. Westerwalbesloh, U. Kleineberg, U. Heinzmann, M. Drescher, and F. Krausz, Science **305**, 1267 (2004).
[14] T. Remetter, P. Johnsson, J. Mauritsson, K. Varju, Y. Ni, F. Lepine, E. Gustafsson, M. Kling, J. Khan, R. Lopez-Martens, K. J. Schafer, M. J. J. Vrakking, and A. L'Huillier, Nature Phys. **2**, 323 (2006).
[15] M. Winter, R. Schmidt, and U. Thumm, Phys. Rev. A **80**, 031401(R) (2009); New J. Phys. **12**, 023020 (2010).
[16] H. Niikura, F. Legaré, R. Hasbani, M. Yu. Ivanov, D. M. Villeneuve, and P. B. Corkum, Nature (London) **421**, 826 (2003).
[17] P. Ranitovic, X. M. Tong, B. Gramkow, S. De, B. DePaola, K. P. Singh, W. Cao, M. Magrakvelidze, D. Ray, I. Bocharova, H. Mashiko, A. Shu, E. Gagnon, M. M. Murnane, H. C. Kapteyn, I. Litvinyuk, and C. L. Cocke, New J. Phys. **12**, 013008 (2010).
[18] F. Kelkensberg, C. Lefebvre, W. Siu, O. Ghafur, T. T. Nguyen-Dang, O. Atabek, A. Keller, V. Serov, P. Johnsson, M. Swoboda, T. Remetter, A. L'Huillier, S. Zherebtsov, G. Sansone, E. Benedetti, F. Ferrari, M. Nisoli, F. Lépine, M. F. Kling, and M. J. J. Vrakking, Phys. Rev. Lett. **103**, 123005 (2009).
[19] B. Feuerstein and U. Thumm, Phys. Rev. A **67**, 063408 (2003).
[20] Th. Ergler, A. Rudenko, B. Feuerstein, K. Zrost, C. D. Schröter, R. Moshammer, and J. Ullrich, Phys. Rev. Lett. **97**, 193001 (2006).
[21] B. Feuerstein, Th. Ergler, A. Rudenko, K. Zrost, C. D. Schröter, R. Moshammer, J. Ullrich, T. Niederhausen, and U. Thumm, Phys. Rev. Lett. **99**, 153002 (2007).
[22] U. Thumm, T. Niederhausen, and B. Feuerstein, Phys. Rev. A **77**, 063401 (2008).
[23] M. Magrakvelidze, F. He, T. Niederhausen, I. V. Litvinyuk, and U. Thumm, Phys. Rev. A **79**, 033410 (2009).
[24] S. A. Aseyev, Y. Ni, L. J. Frasinski, H. G. Muller, and M. J. J. Vrakking, Phys. Rev. Lett. **91**, 223902 (2003).

[25] J. Mauritsson, P. Johnsson, E. Mansten, M. Swoboda, T. Ruchon, A. L'Huillier, and K. J. Schafer, Phys. Rev. Lett. **100**, 073003 (2008).
[26] A. D. Brauk and M. L. Sink, J. Chem. Phys. **74**, 1110 (1981).
[27] P. H. Bucksbaum, A. Zavriyev, H. G. Muller, and D. W. Schumacher, Phys. Rev. Lett. **64**, 1883 (1990).
[28] L. J. Frasinski, J. H. Posthumus, J. Plumridge, K. Codling, P. F. Taday, and A. J. Langley, Phys. Rev. Lett. **83**, 3625 (1999).
[29] M. R. Flannery, H. Tai, and D. L. Albritton, At. Data Nucl. Data Tables **20**, 563 (1977).
[30] We consider linearly polarized XUV pulses and intensities at which the photoelectron angular distribution is best described by a "p-wave", corresponding to the absorption of one XUV photon. Photoemission thus occurs most likely along the XUV electric field direction. In order to include all emission directions, reference to a given emission direction ("left" or "right") is meant to be synonymous with the corresponding ("left" or "right") half space.
[31] D. R. Bates, K. Ledsham, and A. L. Stewart, Philos. Trans. R. Soc. London A **246**, 215 (1953).
[32] K. C. Kuler, F. H. Mies, and K. J. Schafer, Phys. Rev. A **53**, 2562 (1996).
[33] F. He, C. Ruiz, and A. Becker, Phys. Rev. Lett. **99**, 083002 (2007).
[34] F. He, A. Becker, and U. Thumm, Phys. Rev. Lett. **101**, 213002 (2008).
[35] F. He, C. Ruiz, and A. Becker, J. Phys. B **41**, 081003 (2008).
[36] D. Ray, F. He, S. De, W. Cao, H. Mashiko, P. Ranitovic, K. P. Singh, I. Znakovskaya, U. Thumm, G. G. Paulus, M. F. Kling, I. V. Litvinyuk, and C. L. Cocke, Phys. Rev. Lett. **103**, 223201 (2009).
[37] K. P. Singh, F. He, P. Ranitovic, W. Cao, S. De, D. Ray, S. Chen, U. Thumm, A. Becker, M. M. Murnane, H. C. Kapteyn, I. V. Litvinyuk, and C. L. Cocke, Phys. Rev. Lett. **104**, 023001 (2010).
[38] M. F. Kling, C. Siedschlag, A. J. Verhoef, J. I. Khan, M. Schultze, Th. Uphues, Y. Ni, M. Uiberacker, M. Drescher, F. Krausz, and M. J. J. Vrakking, Science **312**, 246 (2006).
[39] R. Gopal, K. Simeonidis, R. Moshammer, Th. Ergler, M. Durr, M. Kurka, K.-U. Kühnel, S. Tschuch, C. D. Schröter, D. Bauer, J. Ullrich, A. Rudenko, O. Herrwerth, T. Uphues, M. Schultze, E. Goulielmakis, M. Uiberacker, M. Lezius, and M. F. Kling, Phys. Rev. Lett. **103**, 053001 (2009).